Sub-arc mantle fugacity shifted by sediment recycling across the Great Oxidation Event

Hugo Moreira[1,2], Craig Storey[2], Emilie Bruand[3], James Darling[2], Mike Fowler[2], Marine Cotte[4,5], Edgar E. Villalobos-Portillo[4], Fleurice Parat[1], Luís Seixas[6], Pascal Philippot[1,7], Bruno Dhuime[1]

[1] Géosciences Montpellier, Université de Montpellier, CNRS, France

[2] School of the Environment, Geography and Geosciences, University of Portsmouth, UK

[3] Geo-Ocean, CNRS, Univ. Brest, Ifremer, France

[4] European Synchrotron Radiation Facility, Grenoble, France

[5] Laboratoire d'Archéologie Moléculaire et Structurale, University of Sorbonne, France

[6] Departamento de Engenharia de Minas, Universidade Federal de Ouro Preto, Brazil

[7] Departamento de Geofísica, Astronomia e Ciências Atmosféricas, Universidade de São Paulo, Brazil

Author information

Corresponding author

Hugo Moreira (hugo.moreira@umontpellier.fr)

Present address: Géosciences Montpellier, Université de Montpellier, CNRS, France

Authors and Affiliations

Géosciences Montpellier, Université de Montpellier, CNRS, France

Hugo Moreira, Fleurice Parat, Pascal Philippot & Bruno Dhuime

School of the Environment, Geography and Geosciences, University of Portsmouth, UK
Hugo Moreira, Craig Storey, James Darling & Mike Fowler

Geo-Ocean, CNRS, Univ. Brest, Ifremer, France
Emilie Bruand

European Synchrotron Radiation Facility, Grenoble, France
Marine Cotte & Edgar E. Villalobos-Portillo

Laboratoire d'Archéologie Moléculaire et Structurale, University of Sorbonne, France
Marine Cotte

Departamento de Engenharia de Minas, Universidade Federal de Ouro Preto, Brazil
Luis Seixas

Departamento de Geofísica, Astronomia e Ciências Atmosféricas, Universidade de São Paulo, Brazil
Pascal Philippot

Abstract:

The chemical exchange between the atmosphere, crust and mantle depends on sediment recycling via subduction. However, it remains unclear how atmospherically-modified sediment may affect mantle oxygen fugacity through time. The Great Oxidation Event, amongst the most significant atmospheric changes on Earth, offers an opportunity to investigate changes in magmatism related to surface-mantle interactions. Here we use Sulphur K-edge micro-x-ray absorption near-edge structure spectroscopy to measure the relative abundances of S^{6+}, S^{4+} and S^{2-} state in apatite inclusions hosted in 2.4-2.1 billion years old igneous zircons from the Mineiro Belt, Brazil. The host magmas record intracrustal melting of juvenile crust and the involvement of recycled sediments in the sub-arc mantle wedge. Unaltered apatite inclusions reveal a change from reduced to more oxidised magmas from pre- to post- Great Oxidation Event during the early Proterozoic. We argue that this change is a direct result of deep subduction of oxidised sediments, and thus evidence of mantle-atmosphere interaction across the Great Oxidation Event. This suggests that the onset of sediment recycling in the Archaean provided atmospheric access to the mantle, and early 'whiffs' of oxygen may have already contributed to a localised increase of calc-alkaline magmatism and related ore deposits on Earth.

Significant accumulation of free oxygen in the atmosphere occurred between ~2.45 and 2.20 billion years ago (Ga)[1–3], with permanent atmospheric oxygenation between 2.3 and 2.2 Ga[4,5]. This period is known as the Great Oxidation Event (GOE) and marks the most dramatic change in Earth's surface chemistry and habitability[6]. However, it remains unclear if these major atmospheric changes affected the amount of free/ chemicallyavailable oxygen in the mantle and, consequently, the redox state of mantle-derived magmas. In the modern Earth, considerable amounts of surface-oxidised components infiltrate the mantle via slab fluids and subducted sediments[7], ultimately influencing the oxidation state of the mantle wedge and arc magmas[8,9]. A better understanding of how magmas changed oxidation through time would clarify ocean-atmosphere influence on mantle redox potential, and whether deep-ocean oxygenation is a feature restricted to the Phanerozoic[10,11].

Mantle oxygen fugacity (fO_2) likely changed in the early Earth as a result of metallic Fe retention during core formation and further homogenization[12,13], but subsequent variations through time are debatable. The mantle fO_2 is either described as largely unchanged[14–16] or overall having a near-constant rate of increase through time[17–20].

Common explanations for the absence of identifiable fO_2 change in the mantle are based on the 'infinite reservoir' argument, given its relatively larger size compared to surface reservoirs (i.e., atmosphere, hydrosphere, and crust[6,15]). Nonetheless, mid-ocean ridge basalts show an increase in the Archaean potentially linked to early 'whiffs' of atmospheric oxygen[18], suggesting that the upper mantle can be affected by changes in the atmosphere. However, despite evidence for recycling of continental materials during at least the past 3.0 Gyr (e.g., ref. [21]), it is unclear how much this has affected the redox state of the mantle, even across the GOE. Here we test the hypothesis of a change in the redox state of magmas in the sub-arc mantle region via recycling processes akin to subduction during the Palaeoproterozoic.

Decoding recycling and oxygen fugacity in the geological record

One of the recognisable changes in the magma record that can provide insights into surface-mantle interactions is the transition from tonalite-trondhjemite-granodiorite (TTG) to sanukitoid magmas recorded in most cratons worldwide[22,23]. This transition started in the Palaeoarchaean and progressed with reduced occurrence to the Palaeoproterozoic[22,24,25]. TTGs are formed by partial melting at depth of (often) altered basaltic rocks, whereas sanukitoids require interaction of TTG like melts and/or sediments within a metasomatized mantle wedge[22,26]. Sanukitoid petrogenesis thus constitutes prima facie evidence for crustal recycling into the upper mantle via 'subduction'[27]. The tectonic settings for this secular magmatic transition are still debated[23,28,29], but all models involve a mechanism that includes a return to the mantle of material that was previously at the Earth's surface (e.g., ref. [30]).

Magmas can contain sulphur in variable valence states (S^{2-}, S^{0}, S^{4+}, S^{6+}), which are chiefly controlled by melting conditions and assimilation of surface material at source[31,32]. The preferential assimilation and fugacity variation of sulphur from mantle source to crustal emplacement is controlled by crystallisation and/or degassing of the magma[33]. As a result, whole-rock analyses of sulphur speciation may involve a large uncertainty due to the volatility and instability of sulphur during and, especially, after crystallisation. This problem is greatly reduced when melt or mineral phase inclusions are analysed as they are protected by the host crystals and therefore more likely to preserve pristine speciation through subsequent tectono-metamorphic-hydrothermal events[34,35].

The accessory mineral apatite has great potential to record sulphur speciation as it can seamlessly incorporate both reduced and oxidised sulphur[36,37] and so retain a proxy for the oxygen fugacity of the crystallising magma[38,39]. Unfortunately, apatite grains easily recrystallise when the host rock is affected by hydrothermal fluids and/or deformation. Hence our approach includes analysing the sulphur speciation of apatite inclusions shielded in host zircon grains and of apatite grains present in the rock's matrix. This avoids secondary alteration processes and offers a robust way to monitor the redox state of the primary magmas (e.g., refs. [40,41,42]). Importantly, U-Pb-Hf isotopes of the host zircon can be used to provide information on the age and the source (i.e., mantle or crustal origin) of the magma from which they crystallised[43], and stable oxygen isotopes can identify a supracrustal component and aqueous alteration at varying temperatures[44,45]. Zircon trace element analyses can also provide insights into the composition and redox state of host magmatic rocks[46]. Thus, combining a multi-isotopic and elemental study of zircon host minerals with extra information on the sulphur speciation of its apatite inclusions is a robust approach to study redox changes in magmas, applied here to those which are primary components of the continental crust.

A Palaeoproterozoic magmatic transition

We investigate samples from two well-characterised suites of intermediate granitoids from the juvenile Mineiro belt, Brazil. These magmatic suites were classified as a 2.35 Ga TTG and 2.13 Ga sanukitoid based on field evidence, geochemistry and isotope studies, both in whole-rock and accessory phases[24,47–49]. They are particularly suitable for this study because they record the youngest transition from TTG to sanukitoid magmatism on Earth, taking place in the Palaeoproterozoic rather than in the Archaean as in many other cratons[23,24]. The transition started shortly before the global 'tectono-magmatic lull' (ref. [50]) and evolved across the time period of irreversible oxygenation of Earth's atmosphere (ref. [5]).

Isotopically, both whole-rock and individual zircon analyses show that the TTGs plot above the chondritic reservoir value (CHUR), and that the sanukitoids have approximately chondritic values[24,49]. This indicates that both magmatic suites have a ‘juvenile’ signature (ref. [43]). Moreover, a projected crustal evolution line typical of granitic crust (^{176}Lu/^{177}Hf = 0.01) demonstrates that the sanukitoid suite can be traced back 200 Myr to the TTG composition, and in turn, those two can be traced back to a depleted mantle source at around 2.5 Ga (**Figure 1a**). Thus, shortly (150 Myr) after mantle extraction, the mafic parental source first underwent partial melting and generated the 2.35 Gyr old TTGs[48]. A similar mafic source was remelted ca. 200 Myr later[47], but this time the magmas record increased depth of melting, as a result of steepening of the subducted slab and opening of a mantle wedge[24]. This second stage generated 2.13 Ga sanukitoid magmas that contain abundant mafic enclaves, with geochemical and oxygen isotope analyses suggesting the involvement of sediments[24] (**Figure 1b**). The absence of any zircon inheritance and chondritic zircon $\varepsilon\mathrm{Hf}_{(t)}$ values alongside substantial range in zircon δ^{18}O (+4.7‰ to +7.5‰), suggests that crustal assimilation is unlikely and the sediments originated from the 2.13 Ga magmatic arc itself – a geological phenomenon described as a ‘self-feeding arc’, where arc sediments form, are deposited in the adjacent ocean and then are subducted[24] (**Figure 1c**). The high concentration of elements that are strongly mobile in aqueous fluids (e.g., Ba and Sr > 1000 ppm) alongside enrichment in mantle-compatible elements (Mg# c. 55, Ni c. 80 ppm and Cr c. 200 ppm; ref. [47]), strongly support sediment admixture in the sub-arc mantle wedge, where sanukitoid magmas were sourced.

The magmas described above evolved within a geologically short duration (2.5 – 2.35 – 2.13 Ga) in an environment akin to intra-oceanic arcs and away from continental sources. Their evolution was nonetheless long enough to witness variations in atmospheric oxygenation consequent upon the GOE. In this context, the intrinsic relationship of the suites as derived from a similar basaltic source remelted at different geological intervals[47–49] suggests that comparative changes of fugacity are feasible.

Sulphur speciation in matrix apatite and inclusions

We have determined the valence(s) of sulphur in apatite using the μ-XANES (X-ray absorption near edge structure) technique at the European Synchrotron Radiation Facility (ESRF) in Grenoble, France (see methods and Supplementary Data). We present 40 analyses in 26 matrix apatite grains, and 136 analyses in 20 apatite inclusions in zircons. For all studied samples, we targeted crack-free apatite inclusions that show no crystallographic misorientation and display a 'hotspot' zone in sulphur concentration maps (**Figure 2**). The patterns show higher sulphur concentration in the centre of the inclusions and gradual decrease towards the host zircon crystal. This core to rim zonation is taken to represent sulphur incorporation and retention during early crystallisation and thus records primary signatures of the crystallising magma. It is unlikely that they represent sulphur exchange with the host, as zircon has negligible sulphur content and extremely slow diffusion rates[51].

Although many apatite inclusions from the 2.35 Gyr old TTG suite have proven to be sulphur barren, six inclusions and a few matrix apatites have sufficiently high sulphur to yield measurable μ-XANES spectra (**Figure 2**); these show remarkably lower S^{6+}/S_{TOTAL} (i.e., they have dominant S^{2-} peak) compared to the apatite sulphur speciation in the 2.13

Ga sanukitoid (**Figure 3**). Matrix apatites and three out of six inclusions have much larger uncertainties and S^{6+}/S_{TOTAL} between 0.4 and 0.7, while analyses of the other inclusions show S^{6+}/S_{TOTAL} <0.1 (**Figure 3**). As matrix apatites are more prone to recrystallisation for not being shielded in zircon, we suggest that these 3 inclusions with much higher S^{6+}/S_{TOTAL} were affected by post-crystallisation interaction with fluids in relative higher fugacity. Moreover, these inclusions with higher S^{6+}/S_{TOTAL} have no detectable 'hotspot' zoning, indicating sulphur redistribution or concentrations straddling the detection limit. One of the analysed inclusions with very low S^{6+}/S_{TOTAL} is hosted by a zircon grain that contains an ilmenite inclusion, reinforcing the interpretation of magmatic crystallisation under possible reduced conditions (**Figure 2**). Ilmenite and magnetite occur in the matrix, but magnetite is thought to have been produced during recrystallisation of the host rock during deformation/metamorphism[48], a process that apparently did not affect the armoured inclusions.

Our results show that matrix apatite grains from the 2.13 Gyr sanukitoid depict a conspicuous oxidised pattern with dominant S^{6+} and high S^{6+}/S_{TOTAL} peak area ratio that is in agreement with apatite inclusions from the same sample (**Figure 2**). The high S^{6+}/S_{TOTAL} for both inclusions and apatite grains in the rock matrix suggests that if any re-crystallisation event has occurred, it was similarly oxidising if compared to the primary fugacity of the inclusions (**Figure 3**). Moreover, magnetite is a common opaque mineral phase in these rocks, formed as isometric homogenous crystals included in hornblende[47], which overall points towards primary oxidising crystallisation conditions.

Quantifying changes in oxygen fugacity

In order to determine fO_2 and ascertain the magnitude of change, we used a sulfur-in-apatite experimental calibration oxybarometer that combines the fayalite-magnetitequartz buffer (FMQ) and S^{6+}/S_{TOTAL} (ref. [39]) (**Figure 3a**). Additionally, we used trace element analyses of the host zircons in a proxy that correlates zircon composition to oxygen fugacity relative to FMQ (ref. [46]). The fO_2 distance from the FMQ buffer (ΔFMQ) is then plotted against the zircon U/Yb to relate to sediment input at source and/or crustal contamination of the magmas (ref. [52]) (**Figure 3b**).

Our results demonstrate that the isotopically and petrologically linked TTG and sanukitoid suites in the Mineiro belt of Brazil crystallised under different redox conditions (**Figure 3**). The 2.35 Gyr old TTG formed when atmospheric oxygen levels fluctuated across a threshold of 10^{-5} of present atmospheric levels (PAL; ref. [53]) and primary apatite inclusions are reduced, with the three most precise measurements ranging from ΔFMQ – 0.75 ± 0.30 to – 0.28 ± 0.38 (2σ standard deviation - average of several analyses within each inclusion, **Figure 3a**). The younger 2.13 Gyr old sanukitoid post-dates the GOE when atmospheric oxygen levels stabilised permanently between 0.1 and 40 % PAL (ref. [54]) and primary inclusions show oxidised sulphur speciation ranging from ΔFMQ + 0.80 ± 0.16 to + 1.24 ± 0.36 (**Figure 3a**). Despite some intergrain variation, trace element analyses in zircons confirm that the 2.13 Gyr old sanukitoid suite is more oxidised than the 2.35 Gyr old TTG, and corroborates the sulphur speciation data in apatite inclusions (**Figure 3b**). The higher U/Yb in zircons from the sanukitoid suite is in agreement with elevated $\delta^{18}O$, and is attributed to surface-derived oxidised sediments that metasomatized the mantle.

An atmospheric window to the mantle

Modern marine sediments can be highly oxidised compared to upper mantle-derived basalts[8]. Their subduction will carry this surficial redox signature and affect the oxidation state of modern arc magmas[7,9]. The generation of a deep subduction-like setting in the Palaeoproterozoic would have facilitated sediment input into the sub-arc mantle source (>10% by volume; ref. [24]). These sediments may have carried sulphate and ferric iron into the mantle wedge in a similar way to that observed in Phanerozoic arcs[10,11]. Oxidised sanukitoid magmas were then formed at 2.13 Ga during melting of a 2.5 Gyr old altered oceanic slab and its sedimentary carapace (**Figure 1**). We suggest that this change in tectonic style allowed the atmosphere to dramatically influence sub-arc mantle chemistry through transfer of oxidised sediments (e.g., refs. [7,9]). The fortuitous occurrence of a TTG-sanukitoid transition in the Mineiro Belt across the GOE has allowed this change in oxidation state to be observed.

The global TTG-sanukitoid transitional record characterises vigorous and protracted crustal recycling and mantle metasomatism in the early Earth (e.g., refs. [22,26]). Although localised and with less magnitude than the GOE, Archaean 'whiffs' of oxygen may have similarly altered the nature of subducted sediments[55], and started to modify the oxygen fugacity of mantle sources in the Archaean (c.f. ref. [42]). It then suggests that similar mantle-surface interactions could have had a major influence on magmatism and metallogenic endowment since the Archaean[56], and that the oxidation of the mantle was diachronous and related to the onset of global plate tectonics. The subsequent irreversible step-rise of oxygen in the Palaeoproterozoic may have led to the dominance of characteristically-oxidised calc-alkaline magmas in the geological record.

Acknowledgments

This project was funded by the European Research Council under the European Union's Horizon 2020 research and innovation program (No. 817934); and CNPq (National

Council for Scientific and Technological Development) grant (234610/2014-0) to H.Moreira. P.P. acknowledges support from the São Paulo Research Foundation (FAPESP 2015/16235-2). We acknowledge the European Synchrotron Radiation Facility for provision of synchrotron radiation facilities through proposal ES-942. We thank Fabrice Barou for assistance with EBSD analyses.

Author contributions

H.M. and C.S. conceived the idea. H.M. performed electron probe and laser ablation analyses. H.M, C.S., E.B., J.D. and B.D., wrote the synchrotron proposal and acquired XANES data. M.F. provided guidance on secular magmatic evolution and sediment-mantle interactions. M.C. coordinated the synchrotron session, validated methodology and data reduction. E.E.V.P. developed the code and reduction protocols for XANES. F.P. provided standards for XANES, conceptual guidance and interpretation of sulphur speciation analysis. L.S. provided field work guidance and validation of the study. P.P. validated interpretations about atmospheric interactions. Original draft was written by H.M. with input and edition from all authors.

Competing interests

The authors declare no competing interests.

Figure captions

Figure 1. Palaeoproterozoic TTG-sanukitoid magmatic transition. a, Zircon U-Pb ages versus ^{176}Hf/^{177}Hf$_{(t)}$ ratios (expressed as εHf$_{(t)}$ values relative to chondrite at the time of crystallisation t). Zircons from TTG magmas (n = 31) have significantly positive

εHf$_{(t)}$ whereas zircons from the sanukitoid magmas (n = 33) are near the chondritic reservoir value (CHUR). A crustal evolution line links both suites of rocks to a depleted mantle (DM) melting event at ~2.5 Ga. **b**, Zircon $^{18}O/^{16}O$ ratios (expressed as $\delta^{18}O$ relative to Vienna Standard Mean Ocean Water) show that the basaltic crust was hydrothermally altered at high temperature (~4.5‰) before generating TTG magmas at 2.35 Ga and before remelting in the metasomatized mantle wedge at 2.13 Ga. The latter event generated sanukitoids that have zircons with heavier oxygen (~6.5‰). Individual error bars in **a** and **b** are shown at 2 standard errors. **c**, Tectonic model for the generation of magmas in the Palaeoproterozic pre- and post- GOE peak. SCLM: subcontinental lithospheric mantle.

Figure 2. Backscattered electron images of inclusions in zircon and sulphur speciation spectra. a–**b**, Twenty-nine μ-XANES analyses in 6 apatite inclusions from the TTG sample and 108 analyses in 14 inclusions from the sanukitoid sample show that the average spectra differ greatly from a reduced (high S^{2-}) speciation in TTG host zircons (**a**) to an oxidised speciation (high S^{6+}) in sanukitoid host zircons (**b**). Inset diagrams show the crystallographic orientation of the inclusions and their relative sulphur concentration.

Figure 3. Oxygen fugacity of the samples studied with respect to the FMQ buffer (ΔFMQ). a, ΔFMQ calculated via $S^{6+}/\Sigma S_{TOTAL}$ oxybarometer proxy. Large dark diamonds are averages of μ-XANES analyses within a single inclusion (sample size as indicated in Fig. 2). Averages of 15 and 25 analyses respectively in 6 matrix apatite grains from the TTG sample (red) and 20 from the sanukitoid samples (blue) are plotted as smaller lighter diamonds. Error bars are 2 standard deviations. **b**, ΔFMQ calculated via zircon

trace element proxy *vs* U/Yb ratios of individual zircon grains from sanukitoid (n = 20) and TTG (n = 23) samples. Error bars are 2 standard errors.

References

1. Philippot, P., Ávila, J.N., Killingsworth, B.A., Tessalina, S., Baton, F., Caquineau, T., Muller, E., Pecoits, E., Cartigny, P., Lalonde, S.V. and Ireland, T.R., 2018. Globally asynchronous sulphur isotope signals require re-definition of the Great Oxidation Event. Nature communications, 9(1), pp.1-10.
2. Warke, M.R., Di Rocco, T., Zerkle, A.L., Lepland, A., Prave, A.R., Martin, A.P., Ueno, Y., Condon, D.J. and Claire, M.W., 2020. The great oxidation event preceded a paleoproterozoic "snowball Earth". Proceedings of the National Academy of Sciences, 117(24), pp.13314-13320.
3. Izon, G., Luo, G., Uveges, B.T., Beukes, N., Kitajima, K., Ono, S., Valley, J.W., Ma, X. and Summons, R.E., 2022. Bulk and grain-scale minor sulfur isotope data reveal complexities in the dynamics of Earth's oxygenation. Proceedings of the National Academy of Sciences, 119(13), p.e2025606119.
4. Luo, G., Ono, S., Beukes, N.J., Wang, D.T., Xie, S. and Summons, R.E., 2016. Rapid oxygenation of Earth's atmosphere 2.33 billion years ago. Science Advances, 2(5), p.e1600134.
5. Poulton, S.W., Bekker, A., Cumming, V.M., Zerkle, A.L., Canfield, D.E. and Johnston, D.T., 2021. A 200-million-year delay in permanent atmospheric oxygenation. Nature, 592(7853), pp.232-236.
6. Lee, C.T.A., Yeung, L.Y., McKenzie, N.R., Yokoyama, Y., Ozaki, K. and Lenardic, A., 2016. Two-step rise of atmospheric oxygen linked to the growth of continents. Nature Geoscience, 9(6), pp.417-424.

7. Ague, J.J., Tassara, S., Holycross, M.E., Li, J.L., Cottrell, E., Schwarzenbach, E.M., Fassoulas, C. and John, T., 2022. Slab-derived devolatilization fluids oxidized by subducted metasedimentary rocks. Nature Geoscience, 15(4), pp.320-326.
8. Kelley, K.A. and Cottrell, E., 2009. Water and the oxidation state of subduction zone magmas. Science, 325(5940), pp.605-607.
9. Padrón-Navarta, J.A., López Sánchez-Vizcaíno, V., Menzel, M.D., Gómez-Pugnaire, M.T. and Garrido, C.J., 2023. Mantle wedge oxidation from deserpentinization modulated by sediment-derived fluids. Nature Geoscience, pp.1-8.
10. Brounce, M., Kelley, K.A., Cottrell, E. and Reagan, M.K., 2015. Temporal evolution of mantle wedge oxygen fugacity during subduction initiation. Geology, 43(9), pp.775-778.
11. Stolper, D.A. and Bucholz, C.E., 2019. Neoproterozoic to early Phanerozoic rise in island arc redox state due to deep ocean oxygenation and increased marine sulfate levels. Proceedings of the National Academy of Sciences, 116(18), pp.8746-8755.
12. Frost, D.J. and McCammon, C.A., 2008. The redox state of Earth's mantle. Annu. Rev. Earth Planet. Sci., 36, pp.389-420.
13. O'Neill, C. and Aulbach, S., 2022. Destabilization of deep oxidized mantle drove the Great Oxidation Event. Science Advances, 8(7), p.eabg1626.
14. Canil, D., 1997. Vanadium partitioning and the oxidation state of Archaean komatiite magmas. Nature, 389(6653), pp.842-845.
15. Li, Z.X.A. and Lee, C.T.A., 2004. The constancy of upper mantle fO2 through time inferred from V/Sc ratios in basalts. Earth and Planetary Science Letters, 228(3-4), pp.483-493.

16. Williams, H.M., Wood, B.J., Wade, J., Frost, D.J. and Tuff, J., 2012. Isotopic evidence for internal oxidation of the Earth's mantle during accretion. Earth and Planetary Science Letters, 321, pp.54-63.
17. Kadoya, S., Catling, D.C., Nicklas, R.W., Puchtel, I.S. and Anbar, A.D., 2020. Mantle data imply a decline of oxidizable volcanic gases could have triggered the Great Oxidation. Nature communications, 11(1), pp.1-9.
18. Aulbach, S. and Stagno, V., 2016. Evidence for a reducing Archean ambient mantle and its effects on the carbon cycle. Geology, 44(9), pp.751-754.
19. Nicklas, R.W., Puchtel, I.S. and Ash, R.D., 2018. Redox state of the Archean mantle: evidence from V partitioning in 3.5–2.4 Ga komatiites. Geochimica et Cosmochimica Acta, 222, pp.447-466.
20. Gao, L., Liu, S., Cawood, P.A., Hu, F., Wang, J., Sun, G. and Hu, Y., 2022. Oxidation of Archean upper mantle caused by crustal recycling. Nature Communications, 13(1), p.3283.
21. Dhuime, B., Hawkesworth, C.J., Cawood, P.A. and Storey, C.D., 2012. A change in the geodynamics of continental growth 3 billion years ago. Science, 335(6074), pp.1334-1336.
22. Martin, H., Moyen, J.F. and Rapp, R., 2009. The sanukitoid series: magmatism at the Archaean–Proterozoic transition. Earth and Environmental Science Transactions of the Royal Society of Edinburgh, 100(1-2), pp.15-33.
23. Laurent, O., Martin, H., Moyen, J.F. and Doucelance, R., 2014. The diversity and evolution of late-Archean granitoids: Evidence for the onset of "modern-style" plate tectonics between 3.0 and 2.5 Ga. Lithos, 205, pp.208-235.
24. Moreira, H., Storey, C., Fowler, M., Seixas, L. and Dunlop, J., 2020. Petrogenetic processes at the tipping point of plate tectonics: Hf-O isotope ternary modelling

of Earth's last TTG to sanukitoid transition. Earth and Planetary Science Letters, 551, p.116558.

25. Bruno, H., Elizeu, V., Heilbron, M., de Morisson Valeriano, C., Strachan, R., Fowler, M., Bersan, S., Moreira, H., Dussin, I., do Eirado Silva, L.G. and Tupinambá, M., 2020. Neoarchean and Rhyacian TTG-Sanukitoid suites in the southern São Francisco Paleocontinent, Brazil: evidence for diachronous change towards modern tectonics. Geoscience Frontiers, 11(5), pp.1763-1787.
26. Nebel, O., Capitanio, F.A., Moyen, J.F., Weinberg, R.F., Clos, F., Nebel-Jacobsen, Y.J. and Cawood, P.A., 2018. When crust comes of age: on the chemical evolution of Archaean, felsic continental crust by crustal drip tectonics. Philosophical Transactions of the Royal Society A: Mathematical, Physical and Engineering Sciences, 376(2132), p.20180103.
27. Fowler, M. and Rollinson, H., 2012. Phanerozoic sanukitoids from Caledonian Scotland: implications for Archean subduction. Geology, 40(12), pp.1079-1082.
28. Martin, H. and Moyen, J.F., 2002. Secular changes in tonalite-trondhjemite-granodiorite composition as markers of the progressive cooling of Earth. Geology, 30(4), pp.319-322.
29. Smithies, R.H., Lu, Y., Kirkland, C.L., Johnson, T.E., Mole, D.R., Champion, D.C., Martin, L., Jeon, H., Wingate, M.T. and Johnson, S.P., 2021. Oxygen isotopes trace the origins of Earth’s earliest continental crust. Nature, 592(7852), pp.70-75.
30. Bédard, J.H., 2018. Stagnant lids and mantle overturns: Implications for Archaean tectonics, magmagenesis, crustal growth, mantle evolution, and the start of plate tectonics. Geoscience Frontiers, 9(1), pp.19-49.
31. Métrich, N. and Mandeville, C.W., 2010. Sulfur in magmas. Elements, 6(2), pp.81-86.

32. Brounce, M., Boyce, J.W. and McCubbin, F.M., 2022. Sulfur in apatite from the Nakhla meteorite record a late-stage oxidation event. Earth and Planetary Science Letters, 595, p.117784.
33. Parat, F., Holtz, F. and Klügel, A., 2011. S-rich apatite-hosted glass inclusions in xenoliths from La Palma: constraints on the volatile partitioning in evolved alkaline magmas. Contributions to Mineralogy and Petrology, 162(3), pp.463-478.
34. Metrich, N. and Clocchiatti, R., 1996. Sulfur abundance and its speciation in oxidized alkaline melts. Geochimica et Cosmochimica Acta, 60(21), pp.4151-4160.
35. Meng, X., Kleinsasser, J.M., Richards, J.P., Tapster, S.R., Jugo, P.J., Simon, A.C., Kontak, D.J., Robb, L., Bybee, G.M., Marsh, J.H. and Stern, R.A., 2021. Oxidized sulfur-rich arc magmas formed porphyry Cu deposits by 1.88 Ga. Nature communications, 12(1), pp.1-9.
36. Parat, F. and Holtz, F., 2004. Sulfur partitioning between apatite and melt and effect of sulfur on apatite solubility at oxidizing conditions. Contributions to Mineralogy and Petrology, 147(2), pp.201-212.
37. Sadove, G., Konecke, B.A., Fiege, A. and Simon, A.C., 2019. Structurally bound S2−, S1−, S4+, S6+ in terrestrial apatite: The redox evolution of hydrothermal fluids at the Phillips mine, New York, USA. Ore Geology Reviews, 107, pp.1084-1096.
38. Konecke, B.A., Fiege, A., Simon, A.C., Parat, F. and Stechern, A., 2017. Co-variability of S6+, S4+, and S2− in apatite as a function of oxidation state: Implications for a new oxybarometer. American Mineralogist, 102(3), pp.548-557.

39. Konecke, B.A., Fiege, A., Simon, A.C., Linsler, S. and Holtz, F., 2019. An experimental calibration of a sulfur-in-apatite oxybarometer for mafic systems. Geochimica et Cosmochimica Acta, 265, pp.242-258.
40. Bruand, E., Fowler, M., Storey, C. and Darling, J., 2017. Apatite trace element and isotope applications to petrogenesis and provenance. American Mineralogist, 102(1), pp.75-84.
41. Bruand, E., Storey, C. and Fowler, M., 2016. An apatite for progress: Inclusions in zircon and titanite constrain petrogenesis and provenance. Geology, 44(2), pp.91-94.
42. Meng, X., Simon, A.C., Kleinsasser, J.M., Mole, D.R., Kontak, D.J., Jugo, P.J., Mao, J. and Richards, J.P., 2022. Formation of oxidized sulfur-rich magmas in Neoarchaean subduction zones. Nature Geoscience, pp.1-7.
43. Kemp, A.I.S., Hawkesworth, C.J., Foster, G.L., Paterson, B.A., Woodhead, J.D., Hergt, J.M., Gray, C.M. and Whitehouse, M.J., 2007. Magmatic and crustal differentiation history of granitic rocks from Hf-O isotopes in zircon. Science, 315(5814), pp.980-983.
44. Valley, J.W., 2003. Oxygen isotopes in zircon. Reviews in mineralogy and geochemistry, 53(1), pp.343-385.
45. Hiess, J., Bennett, V.C., Nutman, A.P. and Williams, I.S., 2009. In situ U–Pb, O and Hf isotopic compositions of zircon and olivine from Eoarchaean rocks, West Greenland: new insights to making old crust. Geochimica et Cosmochimica Acta, 73(15), pp.4489-4516.
46. Loucks, R.R., Fiorentini, M.L. and Henríquez, G.J., 2020. New magmatic oxybarometer using trace elements in zircon. Journal of Petrology, 61(3), p.egaa034.

47. Seixas, L.A.R., Bardintzeff, J.M., Stevenson, R. and Bonin, B., 2013. Petrology of the high-Mg tonalites and dioritic enclaves of the ca. 2130 Ma Alto Maranhão suite: Evidence for a major juvenile crustal addition event during the Rhyacian orogenesis, Mineiro Belt, southeast Brazil. Precambrian Research, 238, pp.18-41.
48. Seixas, L.A.R., David, J. and Stevenson, R., 2012. Geochemistry, Nd isotopes and U–Pb geochronology of a 2350 Ma TTG suite, Minas Gerais, Brazil: Implications for the crustal evolution of the southern São Francisco craton. Precambrian Research, 196, pp.61-80.
49. Moreira, H., Seixas, L., Storey, C., Fowler, M., Lasalle, S., Stevenson, R. and Lana, C., 2018. Evolution of siderian juvenile crust to rhyacian high Ba-Sr magmatism in the Mineiro Belt, southern São Francisco Craton. Geoscience Frontiers, 9(4), pp.977-995.
50. Spencer, C.J., Murphy, J.B., Kirkland, C.L., Liu, Y. and Mitchell, R.N., 2018. A Palaeoproterozoic tectono-magmatic lull as a potential trigger for the supercontinent cycle. Nature Geoscience, 11(2), pp.97-101.
51. Cherniak, D.J. and Watson, E.B., 2003. Diffusion in zircon. Reviews in mineralogy and geochemistry, 53(1), pp.113-143.
52. Grimes, C.B., Wooden, J.L., Cheadle, M.J. and John, B.E., 2015. "Fingerprinting" tectono-magmatic provenance using trace elements in igneous zircon. Contributions to Mineralogy and Petrology, 170(5), pp.1-26.
53. Farquhar, J. and Wing, B.A., 2003. Multiple sulfur isotopes and the evolution of the atmosphere. Earth and Planetary Science Letters, 213(1-2), pp.1-13.
54. Canfield, D.E., van Zuilen, M.A., Nabhan, S., Bjerrum, C.J., Zhang, S., Wang, H. and Wang, X., 2021. Petrographic carbon in ancient sediments constrains

Proterozoic Era atmospheric oxygen levels. Proceedings of the National Academy of Sciences, 118(23), p.e2101544118.

55. Lyons, T.W., Reinhard, C.T. and Planavsky, N.J., 2014. The rise of oxygen in Earth's early ocean and atmosphere. Nature, 506(7488), pp.307-315.

56. Cawood, P.A. and Hawkesworth, C.J., 2015. Temporal relations between mineral deposits and global tectonic cycles. Geological Society, London, Special Publications, 393(1), pp.9-21.

Methods

Sample preparation

Zircons were hand-picked and mounted on tape on a 5 × 5 mm area. A 25 mm diameter round mount was then centred on top of the grains, where epoxy resin was poured and dried in a vacuum chamber. The resin mounts were then polished to reveal the zircons interiors. Cathodoluminesce (CL) and Backscatter Electron (BSE) images for U-Pb, oxygen and Lu-Hf analyses targeting were acquired at the University of Portsmouth. They show oscillatory zoning typical of magmatic grains[24,49]. Host grains and inclusions were identified using elemental mapping by scanning electron microscopy-energy dispersive X-ray spectrometry (SEM-EDS). The spectral composition and 'spot' identification of the different phases were determined using a silicon drift (SDD - EDS) Oxford X-max 80 mm^2 detector attached to a SEM Zeiss EVO MA 10 LaB6 at the University of Portsmouth.

Synchrotron data acquisition and data processing

Sulphur speciation analyses were carried out using the ID21 X-ray microscopy beamline at the European Synchrotron Radiation Facility (ESRF) in Grenoble, France[57]. During the session, the sulphur speciation (S^{-2}, S^{4+} and S^{6+} and their proportions) was measured in both apatite grains and apatite inclusions in zircon. X-ray beam was produced using a 42 period undulator and the energy was selected with a double-crystal monochromator (DCM). XANES spectra were acquired in the range of 2.46 to 2.53 keV, in continuous mode, with steps of 0.2 eV and 0.1s/point, taking approximately 1 minute per point. The calibration of the DCM was done using a gypsum reference powder (maximum of while-line of the XANES spectrum at 2.48184 keV). The fine-tune and focusing was achieved using a set of two Kirkpatrick-Baez (KB) mirrors with a Ni coating. The beam was reduced to 0.3 µm V × 0.4 µm H. Sample mounts were mounted vertically in the microscope, and all measurements were carried out under vacuum (10^{-5} mbar). The beam was then used for construction of 2D µXRF elemental maps and µ-XANES (X-ray absorption near edge structure) spectra for chemical speciation. The detector used was an SGX 100mm^2 SiriusSD silicon drift diode and a multichannel analyzer (MCA). Dead-time of the XRF detector was controlled and beam intensity was attenuated so that DT was always in the range of 17-22% throughout the session. XANES spectra were produced after correction by beam intensity (constantly measured with a photodiode upstream the sample), and the XRF deadtime. Zircon host grains were analysed a few times to assess possible interferences. To separate the XRF K lines from S from the Zr L_2 and L_3 emissions lines, XRF spectra were batch fitted using the PyMca software[58]. Inclusions were located thanks to µXRF map, and appeared as 'hotspot' domains with high sulphur contents. In order to increase the signal to noise of XANES spectra, several points of interest (POI) were selected over each inclusion and an average spectrum was obtained. This approach enables focusing the targets/regions rich in sulphur and optimizes the time spent for each sample.

The ESRF S K-edge XANES spectra inorganic database was used to identify the different peak energy positions for natural minerals with distinct sulphur speciation. To identify S^{6+}(~2482 eV), S^{4+} (~2478 eV) and S^{2-} (~2470 eV) we used gypsum, pyrrhotite and pyrite. The high-focused beam yields high sulphur x-ray counts (in the order of ~ 6000 counts/s for S^{6+} when measuring gypsum and ~4500 counts/s for S^{2-} when measuring pyrite). The same Durango crystal analysed by Konecke et al. (2017) was also analysed during the beginning and at the end of the session and the spectra was reduced as per the unknown apatites. As a similar procedure developed in Konecke et al. (2017), we analysed across the grain perpendicularly to its c-axis. Those comprise 10 points measured twice each, testing therefore homogeneity and beam damage. A single point at the core of the crystal was further analysed 10 times and match individual measurements, reassuring the minor existence of the beam damage for S^{6+} and S^{2-} peaks[59]. Additionally, we analysed the same grain after a rotation of 90 degrees, to assess possible effect of the crystallographic orientation of the apatite. No differences were noticed in the spectra. The same experiment was performed with grain AMT_03_Zr12b, that contains inclusions 1 and 2. XANES data filtering and reduction was done using Python scripts as well as PyMca 5.5.5 software for visualization and selection of the reduction parameters. First, XANES spectra were filtered to exclude noisy spectra. Only spectra with a white line intensity that were at least 2 times higher than the signal measured at the pre-edge background were considered. XANES normalization values were 2.47006 keV for the edge and -0.008840, -0.004420 keV for pre-edge and 0.004550, 0.045496 keV for the post-edge. Spectra were fitted as a linear combination of Gaussian peaks, using a Python code and the advanced fitting from PyMca for Gaussians curves. Finally, the script extracted the peak area ratios (S^{6+}/S_{TOTAL}). The average integrated S^{6+}/S_{TOTAL} peak area ratio obtained for Durango is 0.956 ± 0.004 (2 standard error), in agreement with the peak area ratio obtained by Konecke et al. (2017) (0.956 ± 0.002; 2 standard error).

Electron Backscatter Diffraction (EBSD)

EBSD analyses were performed in zircon, apatite and apatite inclusions to evaluate the microstructural relationship of these phases and the possible relationship between sulphur speciation and crystallographic orientation. Analyses were performed at Géosciences Montpellier, France using a CamScan X500-FEG Crystal Probe. This SEM was developed from its conception for high resolution crystallographic mapping by backscattered electron diffraction. It thus has the particularity of having its electronic column tilted at 70°, which makes it possible to keep the sample horizontal during analyses, and allows backscattered electron diffraction detection of surfaces with uneven polishing. The EBSD Symmetry detector of CMOS technology was used for crystallographic analysis and a detector EDS UltimMax 100 was used for chemical analysis. Reduction of the data was performed using the AZtec software of Oxford instruments. The crystallographic data were processed using *Tango* for orientation map display. Noise reduction was applied to the raw crystallographic data and the final EBSD maps contain the band contrast for quality of the diffraction pattern and lattice orientation of each phase analysed. Within each phase analysed, no misorientation >3° was observed, suggesting high crystallinity of individual phases and that processes of recrystallization are unlikely to have occurred. The small misorientation observed is possibly caused by polishing and hardness of the apatite inclusions against zircon host. These features do not compromise nonetheless the refraction of part of the inclusions and are sufficient enough quality to assess crystallographic orientation. We analysed apatite inclusions with variable crystallographic orientations, which show no correlation in their sulphur μ-XANES spectra (**Figure 2**).

Zircon trace element analysis

Trace element composition was obtained by LA-ICP-MS on distinct zircon domains. Analyses were conducted using an ASI RESOlution Excimer 193 nm laser system, coupled to an Analytik Jena PlasmaQuant Elite ICP-MS at the University of Portsmouth, UK. Laser ablation settings for the first session were 30 μm, 3 Hz and 3.5 J/cm^2. Analyses were located on top of previous EPMA or U-Pb analyses. Oxides formation in the plasma was estimated by monitoring the ThO^+/Th^+ and UO^+/U^+ on the NIST 612 standard, and tuning was done to reach values below 0.3 % and 0.2 % for the ThO^+/Th^+ and UO^+/U^+ ratios, respectively. Elemental fractionation was monitored through repeated measurements of the $^{232}Th/^{238}U$ ratio in NIST 612, with variations between 0.9 and 1 observed during analytical sessions. He carrier gas flow in the ablation cell was set to 0.310 L/min and combined with 0.003 L/min of N_2 gas prior to introduction to the ICP. Plasma generation was set at 1300 W with 10 L/min of Ar plasma flow, auxiliary gas flow of 1.65 L/min and nebulizer flow between 0.89 and 0.9 L/min. The glass NIST 612 was used as a primary standard and zircon reference materials 91500 (ref. [60]), GJ-1 (refs. [61,62]), Plešovice (ref. [63]) and Temora-2 (ref. [64]) were used as secondary standards. The glass NIST 612 was analysed four times at the beginning and at the end of the session and twice each group of unknowns. Each group of unknowns consisted of a combination of four investigated zircons and two secondary standards. The following isotopes were measured and had integration time of 10 ms: ^{25}Mg,^{27}Al, ^{29}Si, ^{31}P, ^{39}K, ^{43}Ca, ^{45}Sc, ^{49}Ti, ^{51}V, ^{53}Cr, ^{55}Mn, ^{85}Rb, ^{87}Sr, ^{89}Y, ^{90}Zr, ^{93}Nb, ^{95}Mo, ^{118}Sn, ^{121}Sb, ^{133}Cs, ^{137}Ba, ^{139}La, ^{140}Ce, ^{141}Pr, ^{146}Nd, ^{147}Sm, ^{153}Eu, ^{157}Gd, ^{159}Tb, ^{163}Dy, ^{165}Ho, ^{166}Er, ^{169}Tm, ^{172}Yb, ^{175}Lu, ^{178}Hf, ^{181}Ta, ^{182}W, ^{208}Pb, ^{209}Bi, ^{232}Th, ^{238}U. The raw data were reduced and corrected for instrumental drift using the Iolite 3.4 software (ref. [65]). Zirconium content was used for internal calibration and measured using a Cameca SX100 electron microprobe at the University of Bristol, UK (see below), avoiding using stoichiometry when normalized. NIST 610 and secondary zircon reference materials yielded results within 10 - 15% in accuracy relative to the recommended published values.

Pressure and temperature dependence

Experimental studies in silicate melts demonstrate that an increase in 100 °C temperature imparts a ΔFMQ – 0.5 deviation in the magma fO_2; whereas an increase in 0.3 GPa would impart a ΔFMQ + 0.2 deviation (refs. [66,67]). Direct measurement of temperature crystallisation via Ti-in-zircon thermometry[68] indicates that zircon grains from the sanukitoid samples crystallised at 800 ± 13 °C (2 standard error) and TTG samples have zircons with average crystallisation temperature of 700 ± 10 °C (2 standard error), considering SiO_2 and TiO_2 activity = 1. A lower TiO_2 activity such as 0.7 yields higher temperatures of crystallisation, 839 °C and 726 °C, respectively for sanukitoid and TTG zircons. Al-in-hornblende oxybarometer indicates crystallisation pressures at around 0.6-0.4 GPa for the sanukitoid samples[47], whereas higher pressure conditions were suggested for the TTG samples (~0.7 GPa) based on the presence of igneous almandine garnet and overall trace element modelling[48]. The ~0.3 GPa difference in pressure between these two magmatic suites is not enough to explain a >1.0 ΔFMQ difference between the calculate fO_2 for sanukitoid and TTG magmas. Moreover, the ~100 °C difference in temperature, if considered, would amplify the contrast in fugacity obtained via sulphur oxybarometry.

Electron probe microanalysis (EPMA)

Zircon grains were analysed by EPMA at the University of Bristol UK using a Cameca SX-100. An electron beam of 5 µm was used with an acceleration voltage of 17 kV and 100 nA beam current. Element concentrations (Si, P, Y, Zr, Yb, Lu, Th and Hf) were determined using TAP, LPET, LLIF and PET crystals. The 91500 zircon standard (ref. [60]) was analysed during the microprobe sessions to monitor data quality. Only analyses with concentrations more than the sum of the individual detection limit and the absolute 2 sigma error were considered. The Zr content was used for internal calibration of trace element analyses presented above and vary from 47-48%.

Data availability

Supporting information for this study is available at https://doi.org/10.6084/m9.figshare.22738082.

Code availability

PyMca 5.5.5 (http://www.silx.org/doc/PyMca/dev/index.html) and Python scripts (https://zenodo.org/deposit/7693613) were used for data visualization and reduction.

Methods-only references

57. Cotte, M., Pouyet, E., Salomé, M., Rivard, C., De Nolf, W., Castillo-Michel, H., Fabris, T., Monico, L., Janssens, K., Wang, T. and Sciau, P., 2017. The ID21 X-ray and infrared microscopy beamline at the ESRF: status and recent applications to artistic materials. Journal of Analytical Atomic Spectrometry, 32(3), pp.477-493.

58. Solé, V.A., Papillon, E., Cotte, M., Walter, P. and Susini, J., 2007. A multiplatform code for the analysis of energy-dispersive X-ray fluorescence spectra. Spectrochimica Acta Part B: Atomic Spectroscopy, 62(1), pp.63-68.

59. Wilke, M., Jugo, P.J., Klimm, K., Susini, J., Botcharnikov, R., Kohn, S.C. and Janousch, M., 2008. The origin of S4+ detected in silicate glasses by XANES. American Mineralogist, 93(1), pp.235-240.

60. Wiedenbeck, M.A.P.C., Alle, P., Corfu, F.Y., Griffin, W.L., Meier, M., Oberli, F.V., Quadt, A.V., Roddick, J.C. and Spiegel, W., 1995. Three natural zircon standards for U-Th-Pb, Lu-Hf, trace element and REE analyses. Geostandards newsletter, 19(1), pp.1-23.

61. Jackson, S.E., Pearson, N.J., Griffin, W.L. and Belousova, E.A., 2004. The application of laser ablation-inductively coupled plasma-mass spectrometry to in situ U–Pb zircon geochronology. Chemical geology, 211(1-2), pp.47-69.

62. Piazolo, S., Belousova, E., La Fontaine, A., Corcoran, C. and Cairney, J.M., 2017. Trace element homogeneity from micron-to atomic scale: Implication for the suitability of the zircon GJ-1 as a trace element reference material. Chemical Geology, 456, pp.10-18.

63. Schoene, B., Latkoczy, C., Schaltegger, U. and Günther, D., 2010. A new method integrating high-precision U–Pb geochronology with zircon trace element analysis (U–Pb TIMS-TEA). Geochimica et Cosmochimica Acta, 74(24), pp.7144-7159.

64. Black, L.P., Kamo, S.L., Allen, C.M., Davis, D.W., Aleinikoff, J.N., Valley, J.W., Mundil, R., Campbell, I.H., Korsch, R.J., Williams, I.S. and Foudoulis, C., 2004. Improved 206Pb/238U microprobe geochronology by the monitoring of a trace-element-related matrix effect; SHRIMP, ID–TIMS, ELA–ICP–MS and oxygen isotope

documentation for a series of zircon standards. Chemical Geology, 205(1-2), pp.115-140.

65. Paton, C., Hellstrom, J., Paul, B., Woodhead, J. and Hergt, J., 2011. Iolite: Freeware for the visualisation and processing of mass spectrometric data. Journal of Analytical Atomic Spectrometry, 26(12), pp.2508-2518.

66. Matjuschkin, V., Blundy, J.D. and Brooker, R.A., 2016. The effect of pressure on sulphur speciation in mid-to deep-crustal arc magmas and implications for the formation of porphyry copper deposits. Contributions to Mineralogy and Petrology, 171(7), pp.1-25.

67. Nash, W.M., Smythe, D.J. and Wood, B.J., 2019. Compositional and temperature effects on sulfur speciation and solubility in silicate melts. Earth and Planetary Science Letters, 507, pp.187-198.

68. Ferry, J.M. and Watson, E.B., 2007. New thermodynamic models and revised calibrations for the Ti-in-zircon and Zr-in-rutile thermometers. Contributions to Mineralogy and Petrology, 154(4), pp.429-437.

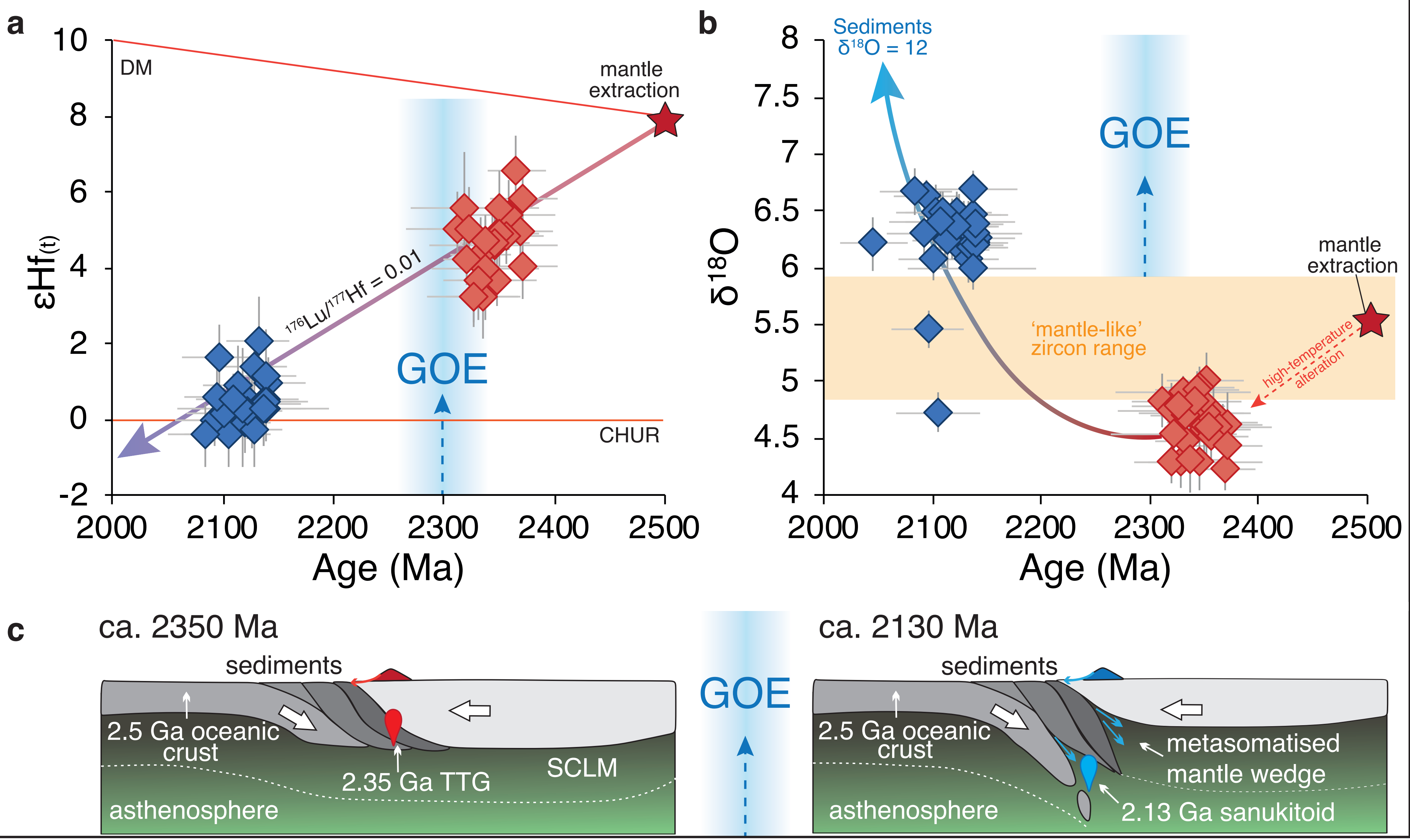
a
10
8
6
4
2
0
-2
$\varepsilon Hf_{(t)}$
DM
mantle extraction
$^{176}Lu/^{177}Hf = 0.01$
GOE
CHUR
2000
2100
2200
2300
2400
2500
Age (Ma)
b
8
7.5
7
6.5
6
5.5
5
4.5
4
$\delta^{18}O$
Sediments $\delta^{18}O = 12$
GOE
mantle extraction
'mantle-like' zircon range
high-temperature alteration
2000
2100
2200
2300
2400
2500
Age (Ma)
c
ca. 2350 Ma
sediments
2.5 Ga oceanic crust
2.35 Ga TTG
SCLM
asthenosphere
GOE
ca. 2130 Ma
sediments
2.5 Ga oceanic crust
metasomatised mantle wedge
2.13 Ga sanukitoid
asthenosphere

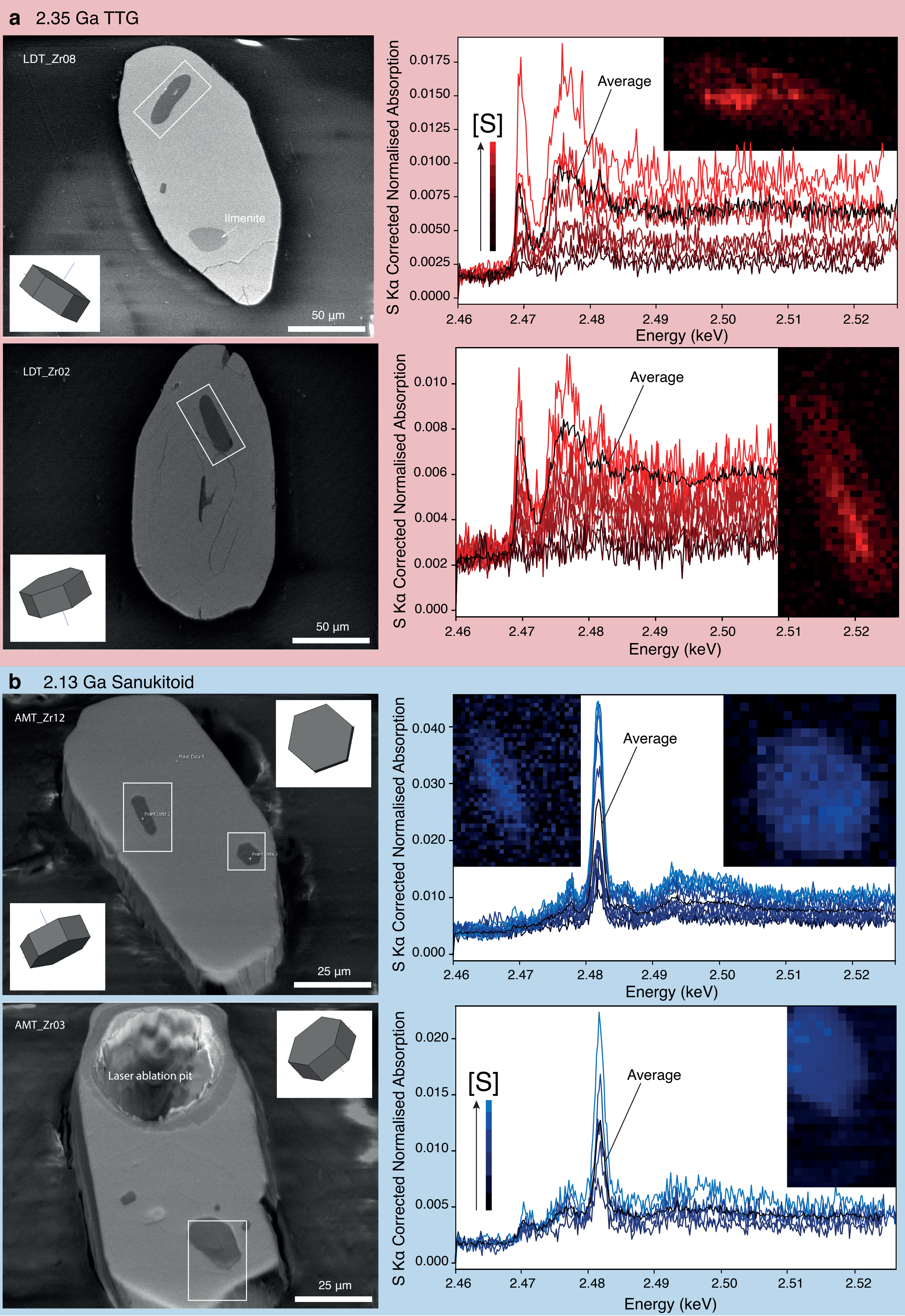
a
2.35 Ga TTG
LDT_Zr08
Ilmenite
50 µm
[S]
Average
S Kα Corrected Normalised Absorption
0.0000
0.0025
0.0050
0.0075
0.0100
0.0125
0.0150
0.0175
2.46
2.47
2.48
2.49
2.50
2.51
2.52
Energy (keV)
LDT_Zr02
50 µm
Average
S Kα Corrected Normalised Absorption
0.000
0.002
0.004
0.006
0.008
0.010
2.46
2.47
2.48
2.49
2.50
2.51
2.52
Energy (keV)
b
2.13 Ga Sanukitoid
AMT_Zr12
Point Data 1
Point Data 2
Point Data 3
25 µm
Average
S Kα Corrected Normalised Absorption
0.000
0.010
0.020
0.030
0.040
2.46
2.47
2.48
2.49
2.50
2.51
2.52
Energy (keV)
AMT_Zr03
Laser ablation pit
25 µm
[S]
Average
S Kα Corrected Normalised Absorption
0.000
0.005
0.010
0.015
0.020
2.46
2.47
2.48
2.49
2.50
2.51
2.52
Energy (keV)

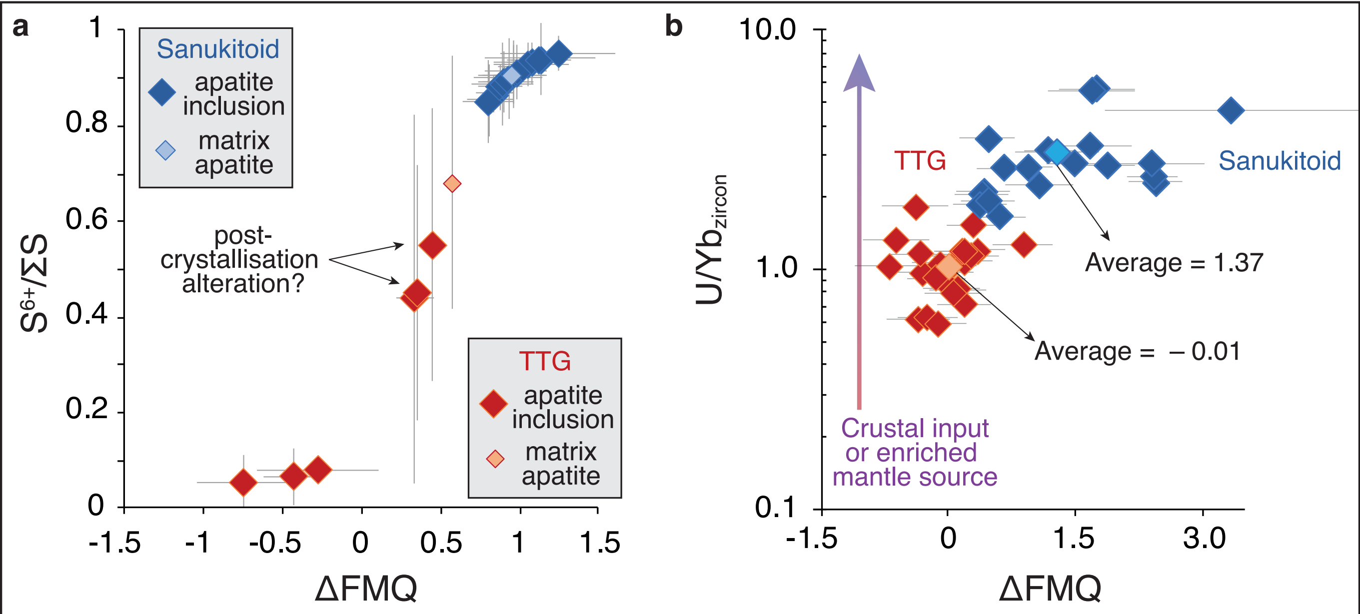
a
Sanukitoid
apatite inclusion
matrix apatite
TTG
apatite inclusion
matrix apatite
post-crystallisation alteration?
$S^{6+}/\Sigma S$
0
0.2
0.4
0.6
0.8
1
-1.5
-1
-0.5
0
0.5
1
1.5
ΔFMQ
b
TTG
Sanukitoid
Average = 1.37
Average = – 0.01
Crustal input or enriched mantle source
U/Yb_{zircon}
0.1
1.0
10.0
-1.5
0
1.5
3.0
ΔFMQ